2015

On the Catalytic Activity of Palladium Nanoparticles-Based Anodes Towards Formic Acid Electro-oxidation: Effect of Electrodeposition Potential

Islam M. Al-Akraa Dr.
The British University in Egypt, islam.ahmed@bue.edu.eg

Ahmad M. Mohammad Prof
Cairo University, ammohammad@cu.edu.eg

Mohamed S. El-Deab Prof
Cairo University, msaada68@yahoo.com

Bahgat E. El-Anadouli Prof
Cairo University, bahgat30@yahoo.com

Chapter 40
On the Catalytic Activity of Palladium Nanoparticles-Based Anodes Towards Formic Acid Electro-oxidation: Effect of Electrodeposition Potential

Islam M. Al-Akraa, Ahmad M. Mohammad, Mohamed S. El-Deab, and Bahgat E. El-Anadouli

Abstract In this investigation, the catalytic activity of palladium nanoparticles (PdNPs)-modified glassy carbon (GC) (simply noted as PdNPs/GC) electrodes towards the formic acid electro-oxidation (FAO) was investigated. The deposition of PdNPs on the GC substrate was carried out by a potentiostatic technique at different potentials and the corresponding influence on the particles size and crystal structure of PdNPs as well as the catalytic activity towards FAO was studied. Scanning electron microscopy (SEM) demonstrated the deposition of PdNPs in spherical shapes and the average particle size of PdNPs deposited at a potential of 0 V vs. Ag/AgCl/KCl(sat.) was the smallest (ca. 8 nm) in comparison to other cases, where the deposition proceeded at higher potentials. The electrochemical measurements agreed consistently with this, where the highest surface area of PdNPs was calculated similarly for the deposition carried out at 0 V vs. Ag/AgCl/KCl(sat.). Interestingly, the X-ray diffraction (XRD) analysis revealed a similar dependency of the PdNPs crystal structure on their particle size and distribution. The deposition of PdNPs at 0 V vs. Ag/AgCl/KCl(sat.) seemed exhibiting the best crystallinity. From the electrocatalytic point of view, the activity of the PdNPs/GC electrode towards FAO decreased with the deposition potential

I.M. Al-Akraa (✉)
Department of Chemical Engineering, Faculty of Engineering, The British University in Egypt, Cairo 11837, Egypt
e-mail: islam.ahmed@bue.edu.eg

A.M. Mohammad • M.S. El-Deab
Department of Chemical Engineering, Faculty of Engineering, The British University in Egypt, Cairo 11837, Egypt

Department of Chemistry, Faculty of Science, Cairo University, Cairo 12613, Egypt
e-mail: ammohammad@cu.edu.eg; msaada68@yahoo.com

B.E. El-Anadouli
Department of Chemistry, Faculty of Science, Cairo University, Cairo 12613, Egypt
e-mail: bahgat30@yahoo.com

I. Dincer et al. (eds.), *Progress in Clean Energy, Volume 1*,
DOI 10.1007/978-3-319-16709-1_40

of PdNPs, which influenced consequently the particle size, shape, and/or crystallographic orientation of PdNPs.

Keywords Palladium nanoparticles • Electrodeposition • Formic acid • Fuel cells • Electrocatalysis • Particle size

40.1 Introduction

Research in fuel cells is intensively growing with the global desire to obtain efficient, incessant, and green energy sources [1, 2]. In this regard, the direct formic acid fuel cells (DFAFCs) have shown superiority over the traditional hydrogen and direct methanol fuel cells (DMFCs) in providing electricity for portable electronic devices [3–5]. The hydrogen fuel cells (HFCs) have long been investigated but the commercialization was restricted by difficulties associated with hydrogen storage and transportation. On the other hand, the DMFCs appeared promising as a consequence of the ease handling (methanol is a liquid fuel) and the high theoretical energy density (approximately 4.9 kWh L^{-1}) of methanol [6]. However, unfortunately, the DMFCs endured an inherent toxicity and a slow oxidation kinetics of methanol as well as the high crossover of methanol through Nafion-based membranes [7]. This has actually drawn attention to find a more convenient fuel for proton exchange membrane fuel cells (PEMFCs). Formic acid (FA) appeared promising in this regard, where it exhibited a smaller crossover flux through Nafion membrane than methanol [8, 9], which, interestingly, allow using high concentrated fuel solutions and thinner membranes in DFAFCs. This is highly desirable for the design of compact portable power systems. Furthermore, DFAFCs have a higher theoretical open-circuit potential (1.40 V) than that of HFCs (1.23 V) and DMFCs (1.21 V) [6, 7]. Nevertheless, DFAFCs experience a severe drawback where the catalytic activity of the Pt anodes (that typically used in DFAFCs), on which FA electro-oxidation (FAO) proceeds, ceases with time. This results from the adsorption of poisoning CO intermediate resulting from the "non-faradaic" dissociation of FA. This ultimately deteriorates the overall performance of DFAFC [3, 4]. Typically on Pt-based materials, FAO proceeds in two parallel pathways; the direct (desirable—involving the dehydrogenation of FA to CO_2 at a low anodic potential), and the indirect (undesirable—involving the chemical dehydration of FA with the release of poisonous CO that next be oxidized by platinum hydroxide at higher potentials (see Eq. (40.1)). Unfortunately, the adsorption of CO on Pt surface in the low potential domain (or the surface poisoning with CO) induces a catalytic deactivation for the electrode, which ultimately impedes the direct route of FAO.

$$\begin{array}{l} \qquad\qquad\quad \text{Pt} + \text{CO}_2 + 2\text{H}^+ + 2\text{e}^- \quad \text{Direct dehydrogenation} \\ \text{Pt} + \text{HCOOH} \\ \qquad\qquad\quad \text{Pt}{-}\text{CO} + \text{H}_2\text{O} \longrightarrow \text{Pt} + \text{CO}_2 + 2\text{H}^+ + 2\text{e}^- \quad \text{Indirect dehydration} \end{array} \tag{40.1}$$

To overcome the electrode's poisoning with CO and to prevent the catalytic deterioration of the electrode's activity, the development of new efficient and stable anodic catalysts for FAO will be necessary. Actually, Pd represents the reference catalyst for FAO where it provides even a better catalytic enhancement than Pt-based materials [10–12]. However, unfortunately, this catalytic activity deteriorates rapidly as a consequence of the poor stability of Pd catalyst [13]. That is why attention was shifted towards Pt-based materials regardless the lower catalytic activity provided. If we could solve the catalytic deactivation of Pd surfaces, it will be much interesting than Pt. The reaction mechanism of FAO on Pd proceeds exclusively via the dehydrogenation pathway (Eq. (40.1)) to produce carbon dioxide (CO_2) with very minor poisoning by CO [13, 14].

$$\mathrm{Pd} + \mathrm{HCOOH} \rightarrow \mathrm{Pd} + \mathrm{CO_2} + 2\mathrm{H^+} + 2e^- \tag{40.2}$$

The Pd catalyst was previously prepared by several approaches such as the dip coating [15], spraying [16], painting [17], sputtering, and electroplating (electrodeposition) [18–20]. Among these techniques, the electrodeposition of Pd catalyst onto a carbon substrate has attracted a particular attention due to the ease of preparation, suitability for special-shaped electrodes and low cost requirement. However, several studies indicated that the potential of electrodeposition may affect the particle size, geometry, and distribution of the Pd catalyst on the electrode surface, which will definitely change the electrochemical surface area and influence the electrocatalytic performance [21, 22].

With the revolution in nano-manufacturing, the use of palladium nanoparticles (PdNPs)-modified catalyst for FAO will be promising in twofold; the materials' saving and, hopefully, overcoming the catalytic deterioration of Pd. However, initially we need to investigate the influence of deposition potential on the particle size distribution and the catalytic activity of PdNPs towards FAO.

In this study, PdNPs will be electrodeposited by a potentiostatic method at different potentials onto GC electrodes to investigate how the deposition potential influences the PdNPs' particle size, crystal structure, and electrocatalytic activity towards FAO. The electrochemical measurements, field-emission scanning electron microscopy (FE-SEM), and X-ray diffraction (XRD) spectroscopy are all combined to reveal the surface morphology, composition, and crystal structure of PdNPs and to understand the origin of enhancement in the catalytic activity of the catalyst.

40.2 Experimental

Typically cleaned glassy carbon electrode (GC, $d = 3.0$ mm) was used as the working electrode. A spiral Pt wire and Ag/AgCl/KCl(sat) were used as the counter and reference electrodes, respectively. All potentials in this study are referenced to Ag/AgCl/KCl(sat). The electrodeposition of PdNPs on the bare GC was carried out in 0.1 M H_2SO_4 solution containing 1.0 mM $Pd(CH_3COO)_2$ (Merck KGaA) via a

constant potential electrolysis technique by holding the potential at 0, 0.05, 0.10, 0.15, and 0.20 V corresponding to overpotentials (η) of –0.80, –0.75, –0.70, –0.65, and –0.60 V, respectively. Overpotentials stated here are relative to the standard potential for Pd^{2+} reduction to Pd^0 which is 0.715 V vs. Ag/AgCl/KCl(sat). All of the chemicals used in this investigation were of analytical grade and used without further purification.

The electrochemical measurements were performed at room temperature (25 ± 1 °C) in a conventional two-compartment three-electrode glass cell using BioLogic SAS potentiostat operated with EC-lab® software. A field emission scanning electron microscope (FE-SEM, QUANTA FEG 250) was employed to evaluate the electrode's morphology. The X-ray diffraction (XRD, PANalytical, X'Pert PRO) operated with Cu target ($\lambda = 1.54$ Å) was used to identify the crystallographic structure of PdNPs. The electrocatalytic activity of the modified electrodes towards FAO was examined in a solution of 0.3 M FA at pH of 3.5 (the pH was adjusted by adding a proper amount of NaOH).

40.3 Results and Discussion

40.3.1 Electrochemical and Materials Characterization

Figure 40.1 shows the cyclic voltammogram (CV) obtained at GC electrode in 0.1 M H_2SO_4 containing 1.0 mM $Pd(CH_3COO)_2$ solution at a scan rate of 20 mV s^{-1}. The potential scan started from 1.05 V to more negative potentials. The absence of the cathodic current at potentials more positive than 0.55 V reveals that the under potential deposition (UPD) in this system has not yet reached and that the electro-crystallization started in the overpotential deposition (OPD) region. This indicates a weak deposit–substrate interaction and recommends the Volmer–Weber growth mechanism for the deposition process [23, 24]. This growth mechanism operates on electrodes with low surface energy as has been observed for the electrodeposition of metals on a GC substrate [24]. Looking inside, a single well-defined cathodic peak (peak a) at ca. 0.2 V was observed and assigned to the Pd deposition. At more cathodic potentials ($E = -0.35$ V), the current increased intensively due to the hydrogen adsorption and evolution. On the reverse (anodic direction) sweep, peak (b) represents the hydrogen desorption and/or oxidation. The backward and the forward scans intersect and a nucleation loop is observed at a potential of ca. 0.3 V. The appearance of such a loop indicates that the deposition of Pd on Pd is easier than on GC [25]. At more positive potential ($E = 0.7$ V), the oxidation peak (c) assigns the dissolution of deposited Pd.

The data of Fig. 40.1 was employed to electrodeposit PdNPs onto the GC electrode in 0.1 M H_2SO_4 containing 1.0 mM $Pd(CH_3COO)_2$ solution via a constant potential electrolysis technique. Figure 40.2a shows the current transients of PdNPs electrodeposition onto GC electrode for 10 s at different applied potentials ($E = 0$,

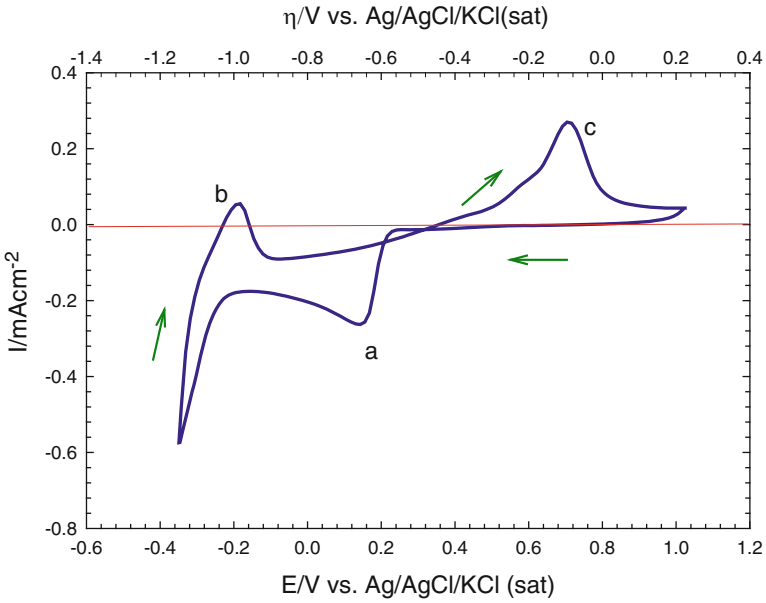

Fig. 40.1 CV obtained at GC electrode in N_2-saturated 0.1 M H_2SO_4 solution containing 1.0 mM $Pd(CH_3COO)_2$. Potential scan rate: 20 mV s^{-1}

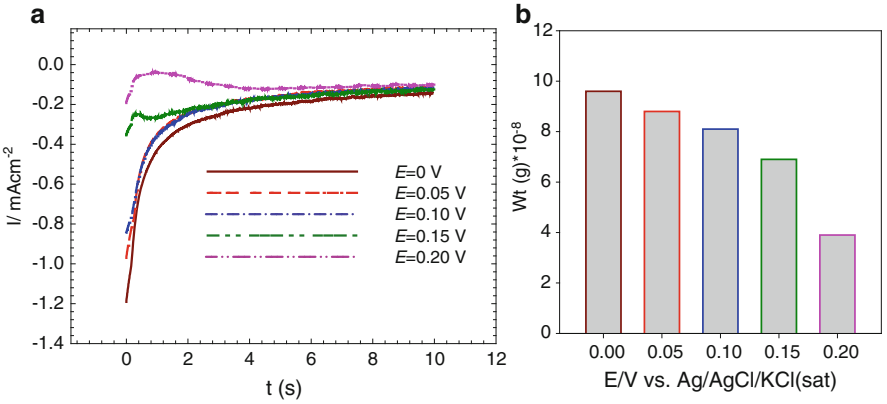

Fig. 40.2 (**a**) Current transients obtained at GC electrode in N_2-saturated 0.1 M H_2SO_4 solution containing 1.0 mM $Pd(CH_3COO)_2$ at different applied potentials ($E = 0$, 0.05, 0.10, 0.15, and 0.20 V), and (**b**) variation of deposited mass of PdNPs with applied electrodeposition potential

0.05, 0.10, 0.15, and 0.20 V). As observed in Fig. 40.2, the charge of deposition decreases with the electrodeposition potential, which will definitely stimulate a consequent decrease in the mass of the deposited PdNPs, as calculated from Faraday's law of electrolysis (see Fig. 40.2b). Actually, not only the mass, but also the particle size, geometry, crystallinity, and electrocatalytic activity of PdNPs

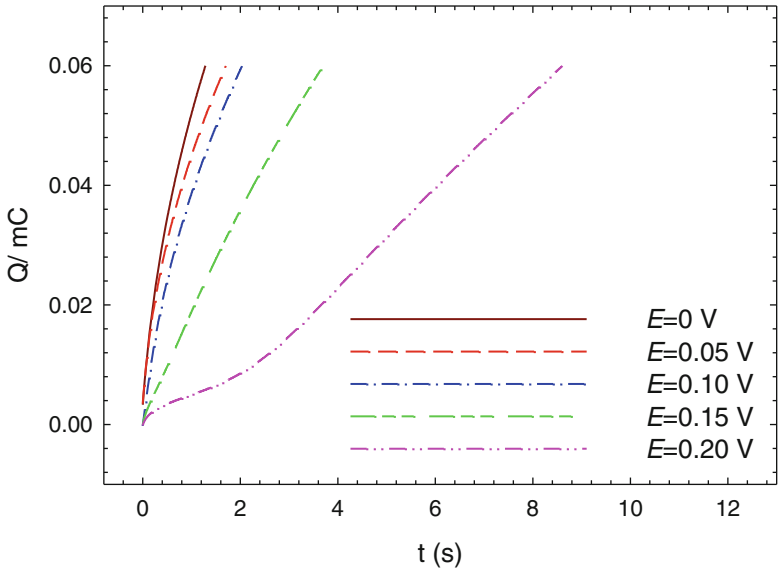

Fig. 40.3 Charge transients obtained at GC electrode in N_2-saturated 0.1 M H_2SO_4 solution containing 1.0 mM $Pd(CH_3COO)_2$ at different applied potentials ($E = 0$, 0.05, 0.10, 0.15, and 0.20 V)

may be influenced by the deposition potential. However, in order to understand precisely this influence, we need to fix the mass of PdNPs deposited at all potentials. This can be achieved if the deposition charge (Q) of PdNPs was kept constant regardless the deposition potential.

Figure 40.3 shows the charge transients of PdNPs electrodeposited onto the GC electrode at different potentials ($E = 0$, 0.05, 0.10, 0.15, and 0.20 V), where Q is kept constant at 60 μC.

As Fig. 40.3 depicts, a deposition time of (1.3, 1.7, 2.1, 3.7, and 8.6 s) was required to pass 60 μC for the deposition of PdNPs with a theoretical net mass of 3.3×10^{-8} g. Now, after avoiding the influence of the catalyst mass, we can investigate the dependence of the particle size, crystallographic structure, and electrocatalytic activity of PdNPs on the deposition potential.

Figure 40.4 shows the characteristic CVs at PdNPs/GC electrode at different applied potentials ($E = 0$, 0.05, 0.10, 0.15, and 0.20 V) applying only a charge of 60 μC. The characteristic behavior of Pd is clearly shown; the oxidation of Pd, which extends over a wide range of potential, is coupled with the oxide reduction peak at ca. 0.50 V. This couple corresponds to the solid-state surface redox transition (SSSRT) involving Pd/PdO. In addition, well-defined peaks for the hydrogen adsorption/desorption are shown in the potential range from 0.0 to −0.2 V. Interestingly, the active real surface area of PdNPs (calculated utilizing the oxide reduction peak at ca. 0.50 V) decreased with the deposition potential, which infers a difference in the particle size and distribution, as long as the mass is

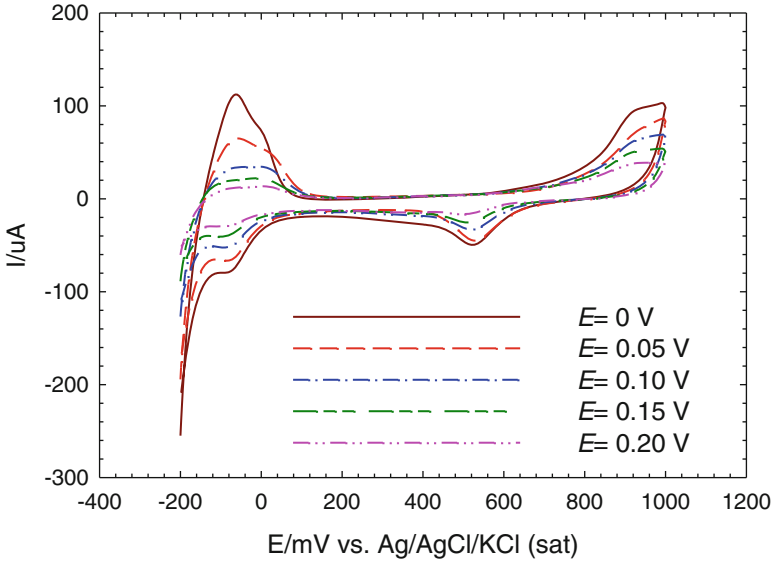

Fig. 40.4 CVs obtained at PdNPs/GC electrode in N_2-saturated 0.5 M H_2SO_4. A same charge of 60 μC is applied at all electrodeposition potentials. Potential scan rate: 100 mV s^{-1}

fixed. A recent report has actually indicated the dependence of the catalyst's particle size on the deposition potential [26].

Interestingly, the deposition of PdNPs at 0 V provided the highest real surface area among the other deposition potentials (see Fig. 40.4). And consequently, we expect the smallest particle size for PdNPs deposited under this potential. This is the role of microscopy to support the assumption. The FE-SEM micrographs in Fig. 40.5 show the corresponding morphology for the set of PdNPs catalysts deposited at 0, 0.10, and 0.20 V. The PdNPs were deposited at 0, 0.10, and 0.20 V in spherical nanoparticles of average particle sizes of ca. 8, 36, and 48 nm, respectively. This agrees very much with our expectation, recommending an increase of average particle size with the increase of the deposition potential. The particles' distribution of PdNPs deposited at 0 V was much more homogeneous if compared to other deposition potentials. It seems with this deposition potential (0 V), the number of individual starting nuclei for PdNPs deposition was higher assisting the uniform distribution of small particles. On the other hand, the deposition of PdNPs at higher potentials favored the deposition of fewer number of PdNPs' nuclei but assisted their rapid growth to end with low density but coarser particles [25].

The influence of the deposition potential on the particle's size of PdNPs may induce a further change in the crystal structure of PdNPs. Recent experiments explained the possibility of changing the lattice parameters of nanoparticles with their particle size, and the dependency became more significant at extremely small particle sizes [27]. The XRD technique was next employ to verify this dependence.

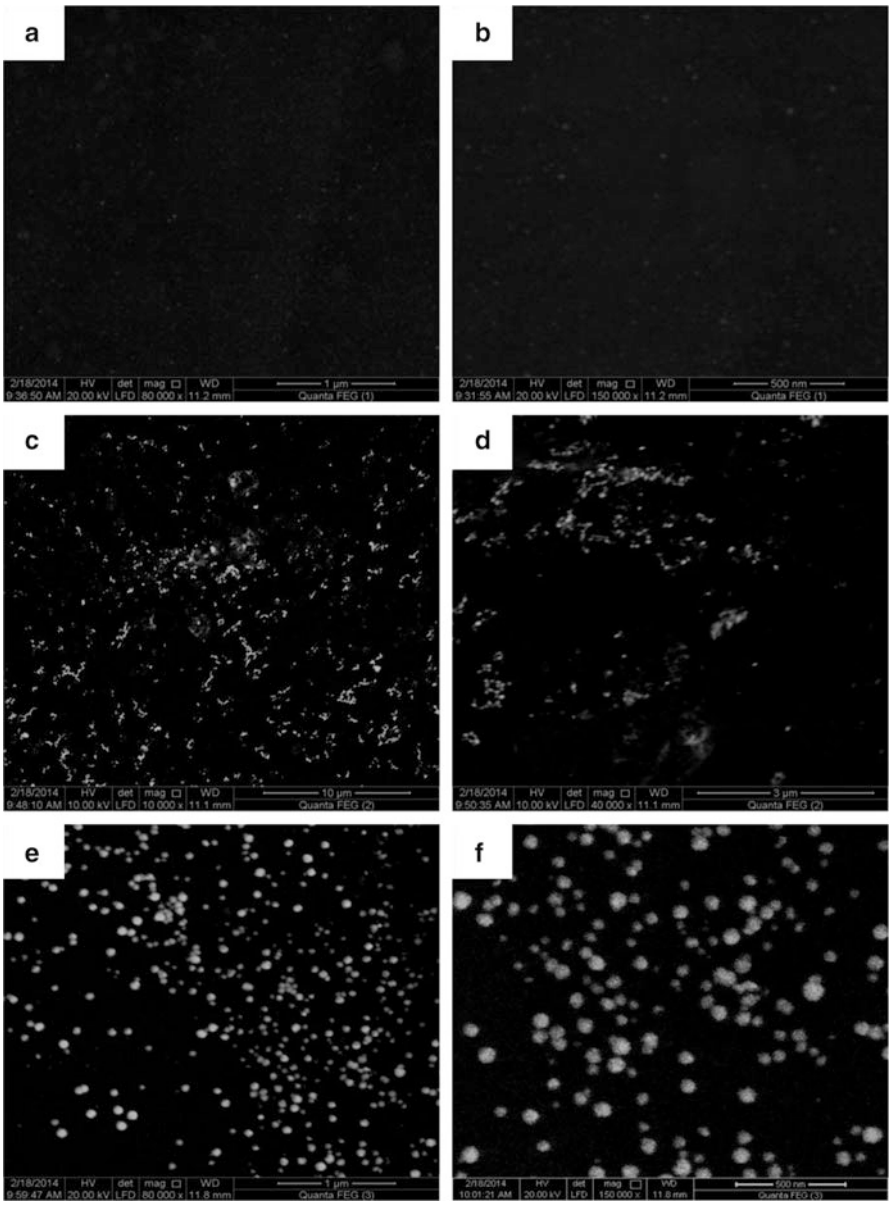

Fig. 40.5 FE-SEM micrographs of PdNPs/GC electrode. The electrodeposition of PdNPs was carried out at (**a**, **b**) 0 V, (**c**, **d**) 0.10 V, and (**e**, **f**) 0.20 V keeping the deposition charge constant at 60 μC

Figure 40.6 depicts the XRD pattern of PdNPs (8, 36, and 48 nm) that were electrodeposited at 0, 0.10, and 0.20 V, respectively. In Fig. 40.6a, the XRD pattern of PdNPs (8 nm) shows several peaks ca. 24°, 38°, 44°, 65°, and 78°. These peaks correspond, respectively, to the (0 0 2) plane of C, (1 1 1), (2 0 0), (2 2 0), and (3 1 1)

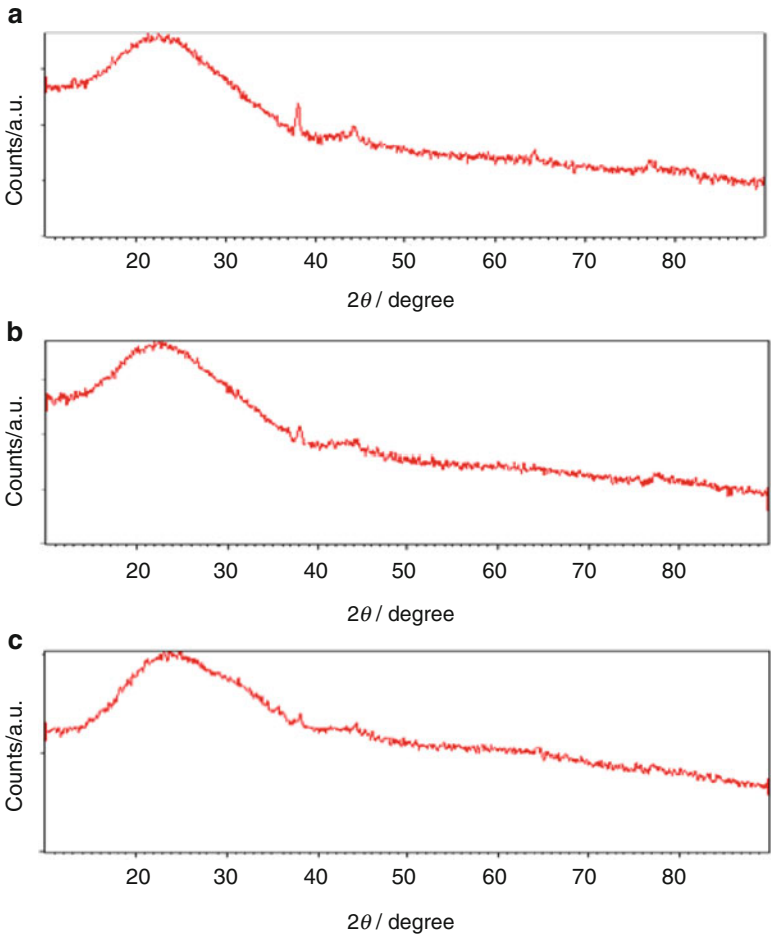

Fig. 40.6 XRD pattern of PdNPs/GC electrode. The electrodeposition of PdNPs was carried out at (**a**) 0 V, (**b**) 0.10 V, and (**c**) 0.20 V keeping the deposition charge constant at 60 μC

planes of Pd face-centered cubic (fcc) lattice (JCPDS standard 05-0681 (Pd)) [21, 28]. However, the intensity of these peaks for PdNPs deposited at 0.10 (36 nm) and 0.20 (48 nm) V was a little bit broad and shorter (Fig. 40.6b and c). This may happen with a certain degree of distortion in the crystal lattice parameters that was associated with the change in the average particle size [29]. The diffraction angles of the lattice planes in Fig. 40.6 were shifted as well to lower values with the decrease in the particle size, which reveals the expansion of the Pd–Pd interatomic distance [28]. The lattice constant of PdNPs, in contrast to other metal nanoparticles, increased with the decrease of particle size, perhaps due to a structural change or incorporation of oxygen, carbon, or hydrogen into the palladium lattice [28]. Table 40.1 summarizes the differences in diffraction angles, interplanar spacing of (1 1 1) plane, and lattice constants of PdNPs deposited at different potentials.

Table 40.1 Differences in diffraction angle (2θ), interplanar spacing (d) of (1 1 1) plane, and lattice constant (a) with PdNPs deposition potential (E), overpotential (η), and PdNPs average size

E (V)	η (V)	Average particle size (nm)	2θ of (1 1 1) (degree)	d (Å)	a (Å)
0	–0.80	8	38.17	2.357	4.082
0.10	–0.70	36	38.23	2.354	4.078
0.20	–0.60	48	38.39	2.344	4.059

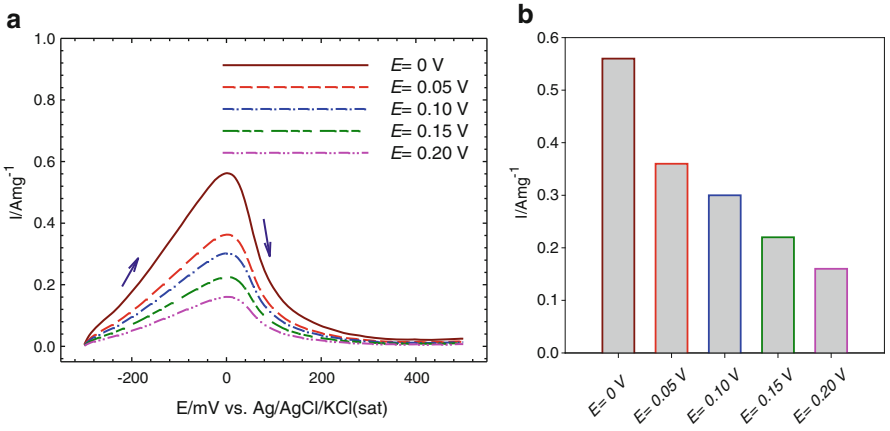

Fig. 40.7 (**a**) LSVs obtained at PdNPs/GC electrode with the same applied charge of 60 μC in N_2-saturated 0.3 M FA (pH 3.5). Potential scan rate: 100 mV s^{-1}, and (**b**) variation of electrocatalytic activity of PdNPs (in terms of oxidation peak specific current) towards FAO with electrodeposition potential

40.3.2 Formic Acid Electro-Oxidation

Figure 40.7a shows the linear sweep voltammograms (LSVs) of FAO at the PdNPs/GC electrode in an aqueous solution of 0.3 M formic acid (pH 3.5), where the deposition of PdNPs was carried out at potentials ($E = 0$, 0.05, 0.10, 0.15, and 0.20 V). A pronounced single oxidation peak is observed at ca. 0 V, which assigns the direct oxidation of FA to CO_2.

The electrocatalytic activity of metal nanoparticles is expected to depend on their size, shape, and crystal structure [30–32]. In our case of PdNPs, the oxidation peak current can be used as a probe to measure the electrocatalytic activity towards FAO. Investigation of these peaks revealed a decrease in the catalytic activity of the PdNPs/GC electrode towards FAO with the increase in deposition potential of PdNPs or with the increase of the average particle size of PdNPs (see Fig. 40.7b). Interestingly, the specific current of the oxidation peak for PdNPs deposited at 0 V was almost 3.5 times larger than that deposited at 0.20 V. As we mentioned previously, the deposition at 0 V resulted in PdNPs with the smallest particle size (8 nm), the highest active real surface area, and the most perfect crystal structure.

Therefore, this deposition condition (0 V) is expected to offer more active sites for the adsorption of FA, which ultimately will lead to a better enhancement in the electrocatalytic activity towards FAO.

40.4 Conclusions

The deposition of PdNPs on the GC electrode was carried out by a potentiostatic technique at different potentials. Electrochemical, SEM, and XRD investigations confirmed that the deposition of PdNPs at a potential of 0 V provided the smallest particle sizes (ca. 8 nm), the largest active surface area, and the most perfect crystal structure for PdNPs. From another view, the electrocatalytic activity of the PdNPs/GC electrode towards FAO decreased with the deposition potential of PdNPs, and the best enhancement was achieved when the deposition was achieved at 0 V. This is definitely attributed to a consequent change in the particle size, distribution, and/or crystallographic orientation of PdNPs.

References

1. Abdullah AM, Okajima T, Mohammad AM et al (2007) Temperature gradients measurements within a segmented H_2/air PEM fuel cell. J Power Sources 172:209–214
2. Abdullah AM, Mohammad AM, Okajima T et al (2009) Effect of load, temperature and humidity on the pH of the water drained out from H_2/air polymer electrolyte membrane fuel cells. J Power Sources 190:264–270
3. Al-Akraa IM, Mohammad AM, El-Deab MS et al (2011) Electrooxidation of formic acid at platinum–gold nanoparticle-modified electrodes. Chem Lett 40:1374–1375
4. Al-Akraa IM, Mohammad AM, El-Deab MS et al (2012) Development of tailor-designed gold-platinum nanoparticles binary catalysts for efficient formic acid electrooxidation. Int J Electrochem Sci 7:3939–3946
5. Zhang S, Shao Y, Yin G et al (2010) Facile synthesis of PtAu alloy nanoparticles with high activity for formic acid oxidation. J Power Sources 195:1103–1106
6. Yu X, Pickup PG (2008) Recent advances in direct formic acid fuel cells (DFAFC). J Power Sources 182:124–132
7. Demirci UB (2007) Direct liquid-feed fuel cells: thermodynamic and environmental concerns. J Power Sources 169:239–246
8. Wang X, Hu J-M, Hsing I-M (2004) Electrochemical investigation of formic acid electro-oxidation and its crossover through a Nafion® membrane. J Electroanal Chem 562:73–80
9. Rhee YW, Ha SY, Masel RI (2003) Crossover of formic acid through Nafion® membranes. J Power Sources 117:35–38
10. Rice C, Ha S, Masel RI et al (2003) Catalysts for direct formic acid fuel cells. J Power Sources 115:229–235
11. Jung WS, Han J, Ha S (2007) Analysis of palladium-based anode electrode using electrochemical impedance spectra in direct formic acid fuel cells. J Power Sources 173:53–59
12. Han SD, Choi JH, Noh SY et al (2009) Performance characterization of direct formic acid fuel cell using porous carbon-supported palladium anode catalysts. Korean J Chem Eng 26:1040–1046

13. Baik SM, Han J, Kim J et al (2011) Effect of deactivation and reactivation of palladium anode catalyst on performance of direct formic acid fuel cell (DFAFC. Int J Hydrogen Energy 36:14719–14724
14. Choi J-H, Jeong K-J, Dong Y et al (2006) Electro-oxidation of methanol and formic acid on PtRu and PtAu for direct liquid fuel cells. J Power Sources 163:71–75
15. Jayashree RS, Gances L, Choban ER et al (2005) Air-breathing laminar flow-based microfluidic fuel cell. J Am Chem Soc 127:16758–16759
16. Gago AS, Morales-Acosta D, Arriaga LG et al (2011) Carbon supported ruthenium chalcogenide as cathode catalyst in a microfluidic formic acid fuel cell. J Power Sources 196:1324–1328
17. Brushett FR, Jayashree RS, Zhou W-P et al (2009) Investigation of fuel and media flexible laminar flow-based fuel cells. Electrochim Acta 54:7099–7105
18. Kjeang E, Michel R, Harrington DA et al (2008) An alkaline microfluidic fuel cell based on formate and hypochlorite bleach. Electrochim Acta 54:698–705
19. Kjeang E, Brolo AG, Harrington DA et al (2007) Hydrogen peroxide as an oxidant for microfluidic fuel cells fuel cells and energy conversion. J Electrochem Soc 154:B1220–B1226
20. Lopez-Montesinos PO, Yossakda N, Schmidt A et al (2011) Design, fabrication, and characterization of a planar, silicon-based, monolithically integrated micro laminar flow fuel cell with a bridge-shaped microchannel cross-section. J Power Sources 196:4638–4645
21. Zhang B, Ye D, Li J et al (2012) Electrodeposition of Pd catalyst layer on graphite rod electrodes for direct formic acid oxidation. J Power Sources 214:277–284
22. Kim H, Subramanian NP, Popov BN (2004) Preparation of PEM fuel cell electrodes using pulse electrodeposition. J Power Sources 138:14–24
23. Alvarez AE, Salinas DR (2010) Formation of Cu/Pd bimetallic crystals by electrochemical deposition. Electrochim Acta 55:3714–3720
24. Komsiyska L, Staikov G (2008) Electrocrystallization of Au nanoparticles on glassy carbon from $HClO_4$ solution containing $[AuCl4]^-$. Electrochim Acta 54:168–172
25. Rezaei M, Tabaian SH, Haghshenas DF (2012) Nucleation and growth of Pd nanoparticles during electrocrystallization on pencil graphite. Electrochim Acta 59:360–366
26. Rezaei M, Tabaian SH, Haghshenas DF (2012) A kinetic description of pd electrodeposition under mixed control of charge transfer and diffusion. J Electroanal Chem 687:95–101
27. Qi WH, Wang MP (2005) Size and shape dependent lattice parameters of metallic nanoparticles. J Nanopart Res 7:51–57
28. Teranishi T, Miyake M (1998) Size control palladium nanoparticles and their crystal structures. Chem Mater 10:594–600
29. Mohanlal SK, Sanjeeviraja C (1986) An X-ray diffraction study of the size effect on a crystalline solid solution of semiconductor system $Ge_{0.2}Si_{0.8}$. Cryst Res Technol 21:K77–K80
30. Kalimuthu P, John SA (2008) Size dependent electrocatalytic activity of gold nanoparticles immobilized onto three dimensional sol–gel network. J Electroanal Chem 617:164–170
31. Hoshi N, Nakamura M, Kida K (2007) Structural effects on the oxidation of formic acid on the high index planes of palladium. Electrochem Commun 9:279–282
32. Zhang L, Sui Q, Tang T et al (2013) Surfactant-free palladium nanodendrite assemblies with enhanced electrocatalytic performance for formic acid oxidation. Electrochem Commun 32:43–46